T. A. Waniewski
Research Scientist,
Naval Hydrodynamics Division,
Science Applications International Corporation,
10260 Campus Point Dr., M/S C4,
San Diego, CA 92121

C. E. Brennen
Professor of Mechanical Engineering

F. Raichlen
Professor of Civil and
Mechanical Engineering

Division of Engineering
and Applied Science,
California Institute of Technology,
Mail Code 104-44
Pasadena, CA 91125

Measurements of Air Entrainment by Bow Waves

This paper describes measurements of the air entrained in experiments simulating the breaking bow wave of a ship for Froude numbers between two and three. The experiments and the characteristics of the wave itself are detailed in T. Waniewski, 1999, ''Air Entrainment by Bow Waves; Ph.D. theses, Calif. Inst. of Tech.'' The primary mechanism for air entrainment is the impact of the plunging wave jet, and it was observed that the air bubbles were entrained in spatially periodic bubble clouds. The void fraction and bubble size distributions were measured in the entrainment zone. There were indications that the surface disturbances described in Waniewski divide the plunging liquid jet sheet into a series of plunging jets, each of which produces a bubble cloud.
[DOI: 10.1115/1.1340622]

1 Introduction

To our knowledge, there are no records in the literature of void fraction and bubble size distribution measurements beneath breaking bow waves in the field, probably because this type of experiment would be exceedingly difficult and costly. There have been, however, studies which measure void fraction and bubble size distributions beneath other types of plunging breaking waves including white caps, and two-dimensional and three-dimensional plunging waves created in laboratory wave tanks. An early example is the measurement of bubble size distributions under white caps by Blanchard and Woodcock [1]. Later, sets of void fraction measurements were made by Lamarre and Melville for two-dimensional plunging waves [2], three-dimensional plunging waves [3], and white caps [4] using impedance-based void fraction instrumentation. They observed that wave breaking creates a bubble cloud which can have a void fraction as high as 30–40 percent. This cloud, primarily comprised of millimeter sized bubbles, then degasses rapidly leaving behind a diffuse plume of microbubbles. Bubble production rates and size distribution measurements for the larger bubbles were made by Cipriano and Blanchard [5] and Loewen et al. [6], among others. Bubble populations in fresh and salt water were compared in studies such as Cartmill and Su [7] and Loewen et al. [6]; bubble plumes in fresh water contain a larger number of smaller bubbles than those in salt water.

Bow waves are continuously breaking plunging waves, and Chanson and Cummings [8] found that the air entrainment process for plunging, breaking waves is similar to that for an inclined plunging jet in cross flow. Studies concerning gas entrainment by plunging liquid jets are summarized in a recent review by Biń [9] show that the nature of the air entrainment process depends on a number of parameters including the flow rate, jet surface turbulence, and jet geometry. Chanson and Cummings [10] use the information from these works to predict the volume rate of air entrainment, bubble sizes, and bubble penetration depth for plunging breakers and demonstrate good comparison with the experimental field data.

Lamarre and Melville [2] showed that the air entrainment process is closely coupled with the breaking wave dynamics, but virtually all of the investigations described above focus on ''two-dimensional'' wave breaking and there is little information on the highly three-dimensional processes which occur in breaking bow waves. The research presented herein used a three-dimensional simulated bow wave, described by Waniewski [11], which allowed for detailed examination of the wave breaking and air entrainment processes. One set of experiments were performed in a 40 m long recirculating flume and are referred to herein as the large flume experiments. The waves were created by a deflecting plate mounted at an angle to the oncoming supercritical flow in the flume. The Froude number of these flows was limited by the flume and ranged from two to three.

2 Experimental Equipment

The 40 m flume is 109 cm wide and 61 cm deep with 1.3 cm thick tempered glass sidewalls and a stainless steel bottom plane to within ±2.5 mm. It was filled with city tap water at about 23°C. Flow rate, Q, is measured using a venturi meter and the depth, d, is measured with a point gage. The maximum discharge is approximately 0.394 m^3/s. To create a super-critical flow, a 20.3 cm high two-dimensional spillway section was installed at the upstream end of the flume, downstream of a 8.1 m long reservoir. The test section is located approximately 24 m (or over 200 depths for the flows investigated) downstream of the spillway. This location ensured a fully developed flow and also gave the air bubbles entrained in the flow downstream of the deflecting plate the maximum time to settle out. Here, a 75 cm long by 50 cm high lucite plate was mounted at an angle θ to the oncoming flow to simulate a wedge shaped hull with half angle θ. The plate's leading edge was machined to a sharp edge and displaced 12 cm from the flume sidewall to reduce the effect of the boundary layer on the wall of the flume. A steady breaking wave, similar to that observed at the bow of a ship, is created as the flow rides up on the plate.

An impedance based void fraction meter (IVFM) was developed to measure the void fraction, α, in these high speed, unsteady, multiphase flows. The IVFM probe, based on a design by Chanson [12] consisted of two concentric stainless steel electrodes, as shown in Fig. 1. The probe tip was aligned with the direction of the bubble velocity, and its small dimensions allowed it to respond to individual bubbles. The impedance across the two electrodes, which increased with void fraction, was mainly resistive for excitation frequencies below the megahertz level. The electronics were designed to detect a 1 mm diameter bubble moving at 2 m/s; therefore, the minimum frequency response required was 4 kHz. The present experiments used 500 kHz excitation at

---

Contributed by the Fluids Engineering Division for publication in the JOURNAL OF FLUIDS ENGINEERING. Manuscript received by the Fluids Engineering Division June 4, 1999; revised manuscript received October 17, 2000. Associate Editors: M. Sommerfeld and J. Katz.

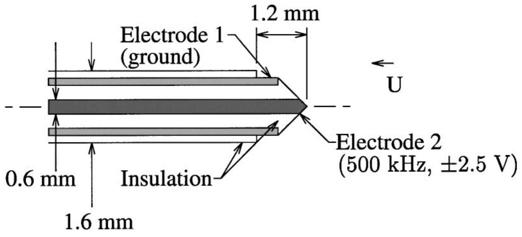

Fig. 1 Cross sectional view of the IVFM probe (not to scale).

the level of ±2.5 V applied to the inner electrode, and the outer electrode was grounded. The output was low-pass filtered with a cutoff of 40 kHz and demodulated to provide a DC signal proportional to the local void fraction.

Single bubble tests were conducted to determine the sensitivity of the IVFM probe to bubble position. The probe was mounted in a tank of water with the tip pointing downward. Single bubbles were intermittently released from a stainless steel tube installed several centimeters below the probe. The bubbles were of uniform 5 mm diameter just before release and deformed as they traveled upward as shown in Fig. 2. The high speed video camera and the IVFM data acquisition system were triggered simultaneously at time $t = 0$ ms. Figure 3 shows the voltage signal corresponding to the images shown in Fig. 2. Correlation of numerous images and voltage signals like these confirmed that a large negative voltage pulse is produced each time a bubble impacted the probe. The pulse width was defined as the time difference between the two crossings of a particular voltage level. The pulse amplitude and width were sensitive to the lateral location of the bubble at impact and this relationship is defined in Waniewski [11].

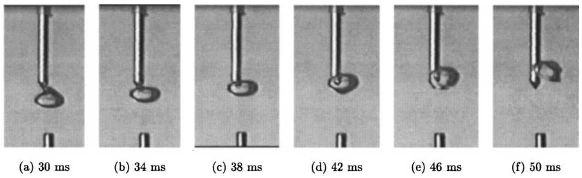

Fig. 2 Frames from high speed video of the single bubble tests showing the IVFM probe tip above the tube which released the bubbles. The time is noted beneath each frame.

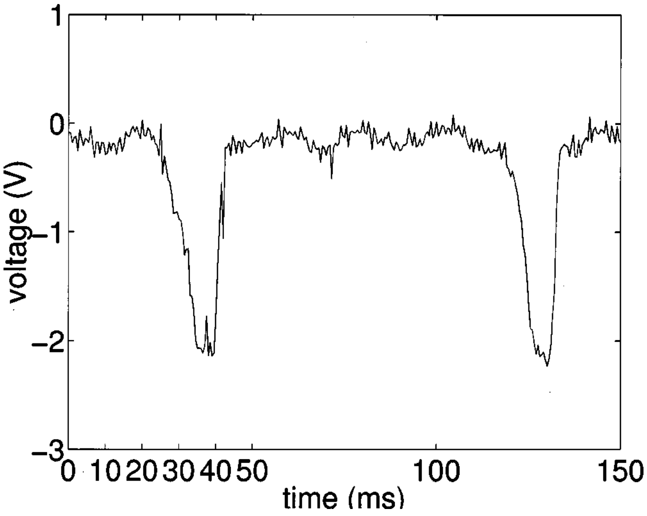

Fig. 3 Typical IVFM signal from the single bubble tests; the frames from the corresponding high speed video are shown in Fig. 2.

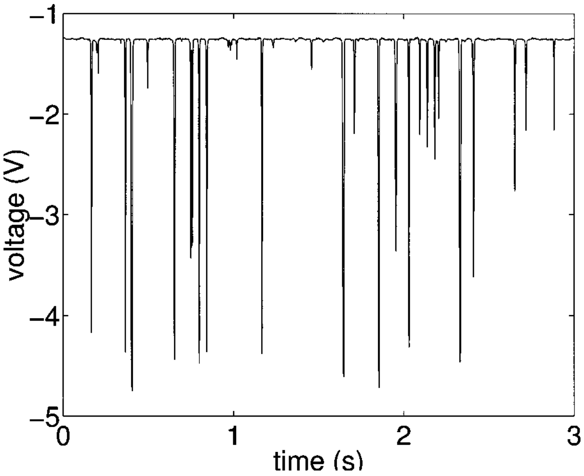

Fig. 4 Typical IVFM signal from the calibration experiments. A voltage of −1.2 V occurs when no air bubbles are touching the probe tip, and each large negative pulse corresponds to an air bubble encounter.

A vertical two-phase flow facility (see Kytomaa [13]) was used to calibrate the IVFM. It included a 10.2 cm working section with an air injector at the lower end. The injector produced air bubbles of uniform diameter of roughly 5 mm. Two static pressure taps located 1.1 m apart, and approximately equally spaced above and below the downward-pointing IVFM probe, were connected to an inverted manometer. The reading from this manometer provided the steady-state void fraction, α. The IVFM signal was sampled at 2 kHz; a typical signal corresponding to $\alpha = 4.31$ percent is shown in Fig. 4. High speed videos confirmed that each pulse corresponded to the impact of a bubble on the probe tip. The IVFM signals were digitally processed using a fourth order Butterworth filter with a cutoff frequency of 1 kHz. Forward and reverse filtering were used to prevent phase distortion, and the mean noise level was subtracted from each signal to compensate for any drift in the IVFM electronics.

The void fraction was calculated from the processed signal using a procedure suggested by Ishii [14] for Eulerian time averaging of two phase flow mixtures. The phases are designated by the subscript k where $k \in \{1,2\}$. The state density function, M_k, for the *kth* phase at location x and time t is defined as taking a value of unity when the *kth* phase is detected and zero when it is absent. The time averaged phase density function or void fraction, α_k, is then given by

$$\alpha_k(x_o, t_o) = \lim_{\delta \to 0} \frac{1}{\Delta t} \int_{[\Delta t]} M_k(x_o, t) dt \qquad (1)$$

where δ is the interfacial region thickness (assumed to be small), x_o is a reference location, and t_o is a reference time. The time interval Δt is fixed and large enough to smooth out local variations in flow properties. Since the actual electronic output was not a simple binary signal, it was necessary to use a threshold output value to convert it to either a zero or unit value of $M_k(x,t)$ so that α could be calculated (Waniewski [11]). Similar methods have been used by other researchers using conductivity probes to measure void fraction (see, for example, Teyssedou et al. [15]).

The calibration was repeated on four different days, and a typical calibration curve is shown in Fig. 5. The void fractions were estimated using three different IVFM signal thresholds. A threshold of −0.75 V gave the best agreement, especially at the lower void fractions as can be seen in Fig. 5.

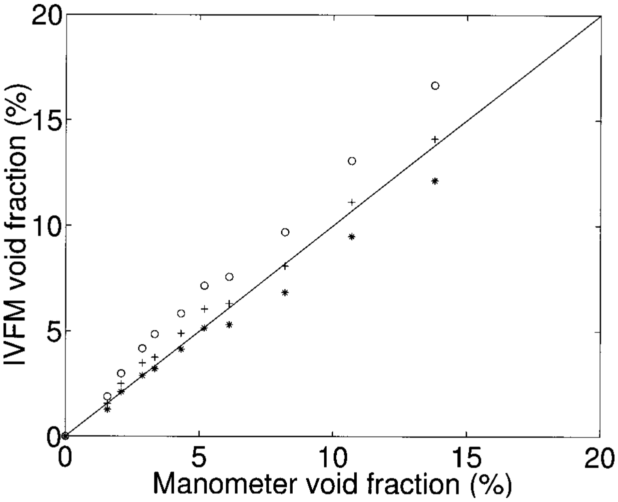

Fig. 5 Calibration data for the IVFM from the bubbly column facility. The different groups of points were produced by processing the same data set using different thresholds; (○) for threshold = −0.50 V, (+) for threshold = −0.75 V, and (*) for threshold = −1.00 V. A linear curve fit for the data corresponding to threshold = −0.75 V also is shown.

3 Experimental Observations

The air entrainment process in the large flume experiments could be observed best when the laboratory was darkened and a stroboscope was positioned to provide a high intensity and short duration, 0.5 μs, light pulse through the window in the bottom of the test section (Waniewski [11]). Observations of the bubbles were made through the glass sidewall of the flume and both direct inspection and high speed movies and videos showed the primary source of air entrainment resulted from the impact of the plunging wave jet on the passing water flow. The resulting splash forms droplets which reimpact causing further entrainment, but this secondary entrainment mechanism will not be addressed here (see, for example, Prosperetti and Oguz [16]).

The plunging wave jet entrained air in ''bursts,'' forming approximately spherical clouds of bubbles visible beneath the free surface. This observation is similar to that of Chanson and Cummings [8] in their experiments on a planar supported jet. For high jet impact velocities (4–8 m/s) they reported a thin layer of air entering the flow at the impact point, adding that the ''air pockets are entrained by discontinuous gusts at the lower end of the air layer.'' In the present experiments, high speed videos revealed that the bubble clouds had a diameter of about 5–10 cm and were comprised of bubbles which were more tightly packed at the center of the cloud than at the edges. Moreover, the formation of these clouds was spatially periodic so that a train of bubble clouds could be observed beneath the free surface at any particular moment in time. A typical photograph of bubble clouds is shown in Fig. 6. Photographs of individual bubbles within the bubble clouds were obtained using a telephoto lens, and though most of the bubbles appeared to be 1–5 mm in diameter, larger finger-like pockets of air also were observed. These did not persist in the clouds; either they were broken up into smaller bubbles by the turbulent flow or they rose to the free surface. Finally, the clouds grew in size as they were convected downstream.

4 Void Fraction and Bubble Size Measurements

For void fraction measurements beneath the simulated bow wave, the IVFM probe was mounted on the carriage described in Waniewski [11]. Measurements were taken at a series of locations in the impact line region of the bow wave plunging jet; one such traverse is shown in Fig. 7. A preliminary series of experiments verified the IVFM signal (see Waniewski [11] for details); a typical signal is presented in Fig. 8. Next, the repeatability of the results was tested. A set of nine IVFM signals were sampled at 20 kHz for 3.2 s at one location under the same circumstances. These had a mean void fraction of 3.2 percent and showed a standard deviation of 0.8 percent thus demonstrating repeatability. Subse-

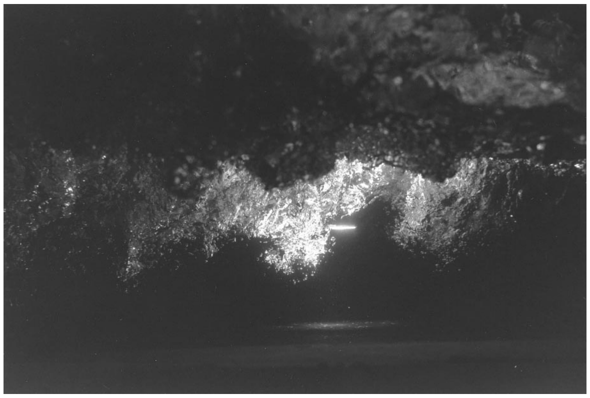

Fig. 6 Photograph of bubble clouds passing by the IVFM probe, the tip of which is visible in the center. The flow is from right to left with $\theta = 25°$, $\phi = 0°$, $U = 2.47$ m/s, $d = 7.39$ cm, and F = 2.90.

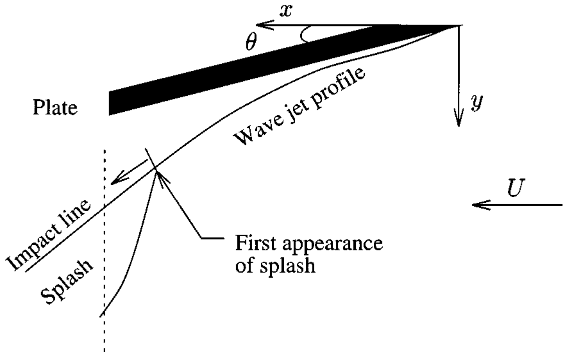

Fig. 7 Schematic diagram of the planform of the flow with a typical IVFM traverse (···) indicated.

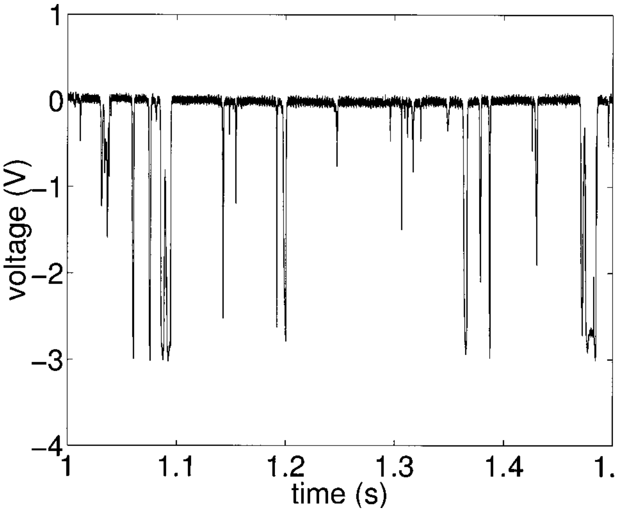

Fig. 8 A typical signal from the IVFM located several centimeters beneath the bow wave plunging jet: $\theta = 26°$, $U = 2.39$ m/s, $d = 6.47$ cm, F = 3.00, and $\alpha = 6.5$ percent.

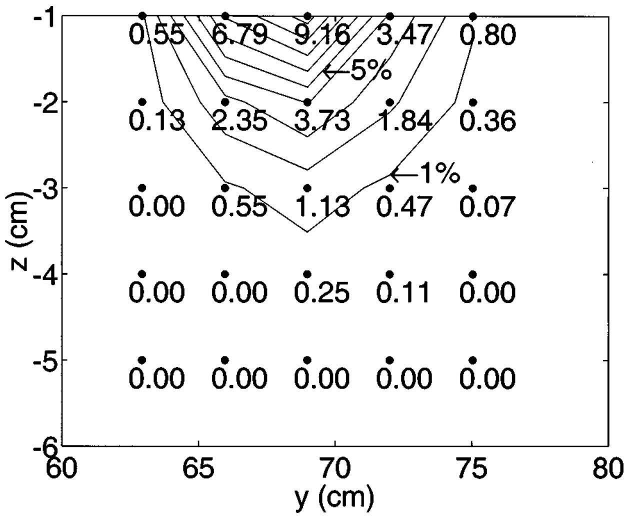

Fig. 9 Local, averaged void fractions beneath the bow wave plunging jet for a traverse at $x=91.2$, and for $\theta=26°$, $\phi=0°$, $U=2.48$ m/s, $d=7.89$ cm, and F=2.82. The IVFM measurement locations are marked (●) and labeled with the void fraction (percent). Nine equally spaced contour levels ($\Delta\alpha=1$ percent) also are shown.

quent measurements were repeated only three times for each location; the mean of the three is reported hereafter.

An example of time-averaged, ensemble-averaged, void fraction data for a traverse as viewed from downstream is shown in Fig. 9. The leading edge of the deflecting plate is located at $(x,y)=(0,0)$ and the upstream free surface is located at $z=0$. Void fraction contours were constructed and highlight the trends in the data. Because the free surface was unsteady, it was not possible to estimate the void fraction at locations above $z=-1$ cm without the free surface dipping below the probe or the probe entraining air. In addition, there is a surface proximity effect for this type of void fraction instrumentation which is described in Lamarre and Melville [3].

Figure 10 shows the void fraction contours for sets of traverses and confirms observations from the high speed video. First, the bubble clouds are shown to be roughly circular in cross section and grow as they convect downstream. Second, the bubbles are more tightly packed at the cloud center than at the edges. The center of the cloud, the region with greatest void fraction, was located directly beneath the impacting jet.

The void fraction mappings in Fig. 10 also were used to calculate the total volume of air entrained at particular streamwise locations. The areas between pairs of consecutive void fraction contours were calculated and multiplied by the void fraction in those regions. A trapezoidal summation of these terms gave the total volume of air, V_{air}, per unit streamwise distance. Note that this is a conservative estimate, since the void fraction was greater than 10 percent for some regions within the cloud but could not be measured accurately. The results for the traverses of Fig. 10 are included in Fig. 11 where $x^*=0$ corresponds to the origin of the impact line. The data for the two sets of flow conditions appear to be consistent with one another despite the slight offset which was within the repeatability of the experiments. Moreover, the data clearly shows that the quantity of air contained in the bubble clouds increases with the distance downstream of the impact line origin. The slope of the quadratic fit in Fig. 11 was used to calculate the volume rate of air entrainment, Q_{air}, for a given bubble cloud where

$$Q_{\text{air}}=Ud_c\frac{dV_{\text{air}}}{dx^*}$$

and d_c is the diameter of the bubble cloud. At location $x^*=10$ cm, typical clouds were 7 cm in diameter and the above expression yielded a Q_{air} of 62 cm^3/s.

The same IVFM signals were used to produce bubble chord distributions for the bubbles which comprised the bubble clouds. The typical dimension of the individual bubbles was represented by a quantity called the bubble chord, l, calculated using $l=U\Delta T$ where ΔT is an individual pulse width in the IVFM signal. Note that since very small bubbles remain spherical, this chord should be close to the bubble diameter. Similar bubble chord calculations for a dual tip conductivity probe are described by Chanson [17] Bubble chord histograms were compiled using bin size of 2 mm. Separate measurements at the same location demonstrated that the histograms were repeatable (Waniewski [11]).

Figure 12 presents typical bubble chord histograms for bubble clouds that passed through the traverse shown in Fig. 10(*d*). Note that most of the bubble chords were 1–7 mm, consistent with the high speed video observations of the size of the individual bubbles. Note also that the number of bubbles in this size range increased from the edge to the center of the cloud and from the bottom to the top of the cloud. Larger pockets of air existed in the center of the cloud near the free surface, giving rise to the larger bubble chords registered at those locations.

5 Frequency of Bubble Cloud Encounters

As described in Section 3, the formation of the bubble clouds was observed to be spatially periodic. Since the clouds convect downstream with the mean flow velocity, they pass a particular location at some specific frequency. High speed video of the bubble clouds was used to estimate this frequency of cloud encounters with the IVFM probe. Each frame of the video was examined, and it was noted whether or not a bubble cloud was present at the probe tip. Frequencies of cloud encounters for flow conditions similar to those in Fig. 8 were between 7 and 14 Hz.

A signal processing technique was implemented to extract the same information from the IVFM signals. This required a quantitative definition of a cloud, and so it was assumed that two bubbles located 1 cm or less apart belong to the same bubble cloud since the clouds were about 10 cm in diameter. If two bubbles are separated by 1 cm in the streamwise direction and move at the mean flow velocity then the time delay between the two bubbles as they impact the IVFM probe tip can be calculated. The IVFM signal was processed using an algorithm which searched for successive pulses caused by individual bubble impacts occurring within this time delay. Figure 13 shows the result of this cloud detection algorithm for a typical IVFM signal. The lower graph shows the reciprocal of the time delay, or frequency of individual bubble impacts with the IVFM probe, as a function of time. To count the clouds, a particular individual bubble impact frequency was chosen as a threshold. Since the mean flow velocity was 2.39 m/s, a threshold of 200 s^{-1} implied that two bubbles belonging to the same cloud could have had a maximum separation distance of 1.2 cm. This threshold also is shown in the lower graph, and a cloud was counted for each local maximum greater than 200 s^{-1}. Note that this technique does not count bubble clouds for which only a single bubble impacted the probe tip; therefore, it gives a lower bound for the frequency of bubble cloud encounters.

The frequency of bubble cloud encounters as a function of depth also was explored (Waniewski [11]). Since the bottom edge of the bubble clouds was lower in void fraction, there was a greater chance at larger depths that only a single bubble would impact the IVFM probe and the algorithm would not count the cloud because the same threshold was maintained for all depths. Hence, the cloud frequency decreased with depth. Near the surface, the typical cloud frequencies measured were 15 Hz as illustrated by Fig. 13; this frequency is similar to those obtained earlier from the high speed video. When compared with the frequency of

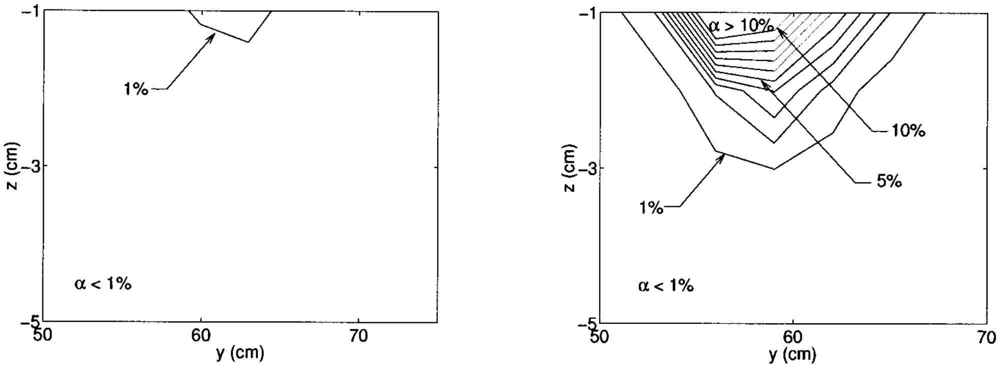

(a) $x = 73.4$ cm, $x^* = 4.4$ cm; plunging jet impacts at $y \approx 63$ cm.

(b) $x = 70.8$ cm, $x^* = 17.8$ cm; plunging jet impacts at $y \approx 56$ cm.

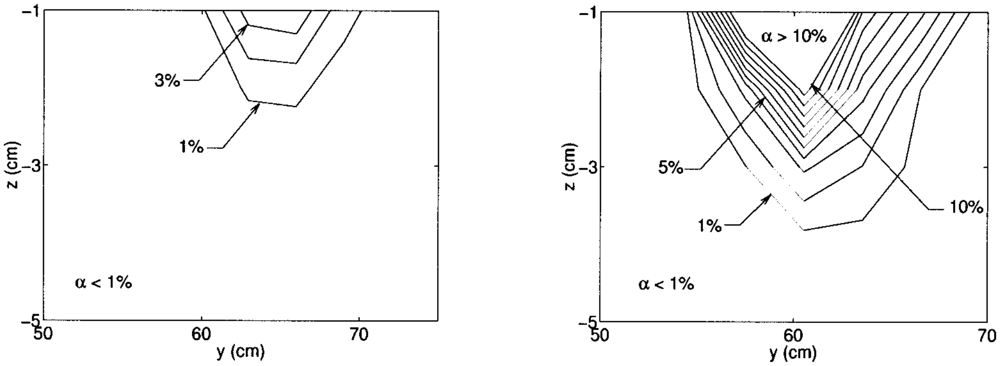

(c) $x = 81.0$ cm, $x^* = 12.0$ cm; plunging jet impacts at $y \approx 65$ cm.

(d) $x = 75.9$ cm, $x^* = 22.9$ cm; plunging jet impacts at $y \approx 60$ cm.

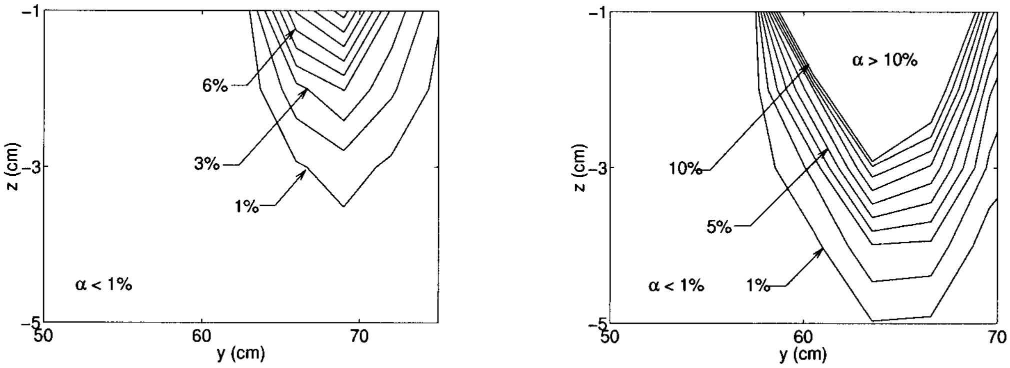

(e) $x = 91.2$ cm, $x^* = 22.2$ cm; plunging jet impacts at $y \approx 69$ cm.

(f) $x = 84.2$ cm, $x^* = 31.2$ cm; plunging jet impacts at $y \approx 64$ cm.

Fig. 10 Local, averaged void fractions for six different traverses: (*a*), (*c*), and (*e*) for the flow conditions specified in Fig. 9 and (*b*), (*d*), and (*f*) for $\theta=26°$, $\phi=0°$, $U=2.39$ m/s, $d=6.47$ cm, and F=3.00. Ten equally spaced contour levels ($\Delta\alpha=1$ percent) are shown.

impact by individual bubbles on the IVFM probe, the number of individual bubble impacts per cloud was calculated to be between three and five.

6 Discussion of Bubble Cloud Formation

Surface disturbances exist on the plunging face of the bow wave because of various flow instabilities, and each surface disturbance leads to an individual plunging jet. These individual jets may or may not break up into a string of droplets before impact. As discussed in Waniewski [11], the individual jets are convected downstream with the mean flow velocity and each entrains air at the point where it impacts the lower water surface. Observations of the bubble clouds beneath the free surface show small bubble clouds formed at the first location where the plunging wave jet

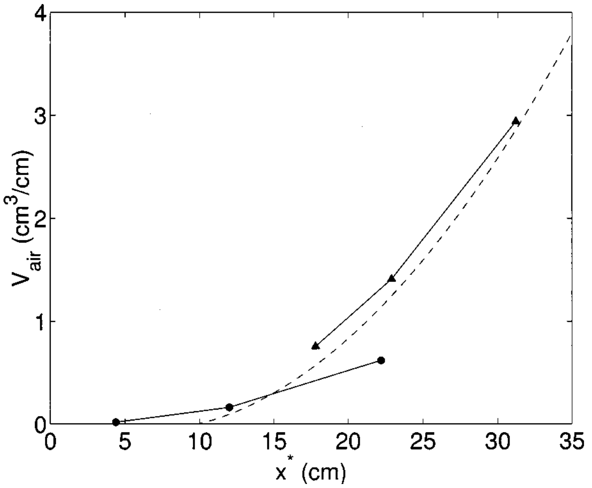

Fig. 11 Total volume of air entrained per unit streamwise distance as a function of distance from the origin of the impact line, x^*; (●) for the traverses of Fig. 10(*a*), (*c*), and (*e*) and (▲) for those of Fig. 10(*b*), (*d*), and (*f*). A quadratic curve fit (- -) also is shown.

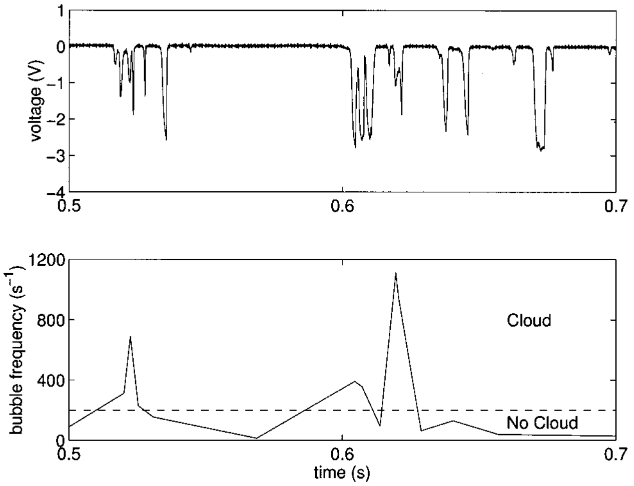

Fig. 13 Detail of signal processing technique. Upper: raw IVFM signal. Lower: cloud detection algorithm output, frequency of individual bubble impacts, from the IVFM signal.

impacts the free surface. These clouds grow in size (observed in high speed video and measured by IVFM) and increase in void fraction (measured by IVFM) as they convect downstream in a direction which follows the impact line of the bow wave.

On the basis of these observations, a mechanism for air entrainment is proposed and is shown schematically in Fig. 14. Each of the individual plunging wave jets entrains air into its own bubble cloud. These jet-cloud structures convect downstream with the mean flow velocity; therefore, the distance between successive surface disturbances determines the distance between bubble clouds. This is consistent with the visual observations of the clouds since dividing the mean flow velocity by the spacing between the disturbances yields the same 20 Hz frequency manifest in the bubble cloud train. Cross-correlations of the IVFM and wave gage signals also seemed to support this hypothesis (Waniewski [11]). In addition, the void fraction increases with downstream distance since more bubbles are injected over time. Simultaneously, the cloud size increases with downstream distance as a result of turbulent mixing.

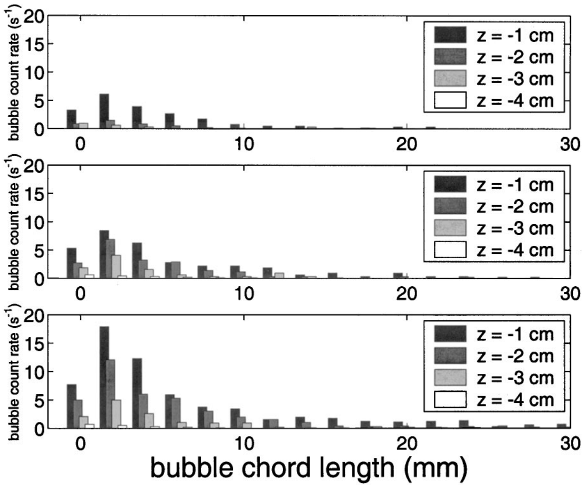

Fig. 12 Bubble chord histograms from bubble clouds observed at x=75.9 cm for different elevations. Upper: y=66.6 cm. Middle: y=63.5 cm. Lower: y=60.5.

We now compare the typical rate of air entrainment measured in these experiments, 62 cm^3/s (see Section 4), with that which might be expected using existing theories. Van de Sande and Smith [18] model air entrainment by low velocity (2–5 m/s) turbulent water jets plunging into a quiescent pool of water and obtain:

$$Q_{\mathrm{air}} = 0.021 \frac{d_j^{3/2} U_j^2 l_j^{1/3}}{\sin(\beta)} \quad m^3/s \tag{2}$$

where Q_{air} is the volume rate of air entrainment, d_j is the jet diameter, U_j is the jet velocity, l_j is the jet length, and β is the jet impingement angle. Using the experimental data presented in Waniewski [11]: $d_j = 3.8$ cm, $U_j = 2.3$ m/s, $l_j = 23$ cm, and $\beta = 58°$, Eq. (2) yields a Q_{air} of 600 cm^3/s. This discrepancy with the measured 62 cm^3/s, was expected. Figure 10 shows that most of the air exists in the >10 percent core and in the $-1 < z < 0$ cm surface layer; however, this air was not included in the 62 cm^3/s. The void fraction in the core was approximated as 10 percent and no approximation was made for the air in the surface layer. The error from these approximations could well account for the difference. On the other hand, it is likely that the air in the core and surface layer out-gasses to the surface quite quickly and the measured Q_{air} of 62 cm^3/s is a better indication of the bubble entrainment which persists further downstream.

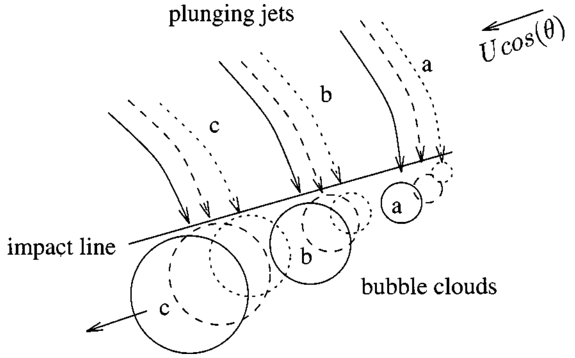

Fig. 14 Schematic diagram of the proposed air entrainment mechanism. A time series of plunging jets and bubble clouds is depicted; (···) for t=0, (- -) for t=Δt, and (—) for t=2Δt.

One of the uses of these data and/or model would be to improve the two-phase flow computations around surface ships. In the absence of such input, Carrica et al. [19] assumed that for an arbitrary area near the bow, a mixture of water and air with a void fraction of 10 percent entered the flow with a constant downward velocity. They further assumed the bubble size distribution measured by Cartmill and Su [7]. The present paper would suggest the following improvements. The location of the air entrainment should be along the impact line only, and the void fraction as a function of the distance along the impact line should be specified consistent with the present data. A similarly consistent bubble size distribution from an average of experimental measurements should be used. Even though the size distributions were seen to vary with location in the present study, most of the bubble chords were between 1 and 7 mm. The velocity of these bubbles entering the flow at the free surface should be the vector sum of the plunging wave jet velocity and the downstream velocity as described in Waniewski [11]. As more detailed models became appropriate, the periodicity observed in the bubble clouds could be included.

7 Conclusions

The primary mechanism for air entrainment in the present bow wave experiments was the impact of the plunging wave jet. Observations of the air entrainment process were made during experimental simulations of a bow wave in a flume which used a high speed video camera with a synchronized strobe lamp. An impedance based void fraction meter (IVFM) was developed specifically to measure void fraction and bubble size distributions beneath this breaking wave.

It was observed that the air is entrained in spatially periodic bubble clouds, approximately 5–10 cm in diameter. The IVFM signals were processed using a cloud detection algorithm to find the rate of bubble cloud encounters. For depths between 1 and 3 cm beneath the free surface, the bubble cloud rates varied from 5–20 Hz. The bubble cloud void fraction could exceed 10 percent in the center of the cloud, and the bubble chords for the bubbles comprising the clouds were between 1 and 7 mm. Void fraction mappings for different flow cross sections beneath the wave were generated, and the bubble chord distributions were calculated for these locations. The void fraction mappings were used to estimate the quantity of air entrained at different streamwise locations. It was found that for a given flow condition, the void fraction increases with the distance traveled along the impact line.

In addition, it appears that the frequency of the surface disturbances, described in detail in Waniewski [11], controls the frequency of the bubble clouds. The surface disturbances divide the plunging liquid jet sheet into a series of individual plunging jets, and each jet entrains air into its own bubble cloud beneath the free surface. This is supported by comparison of the predicted volume rate of air entrainment, Q_{air}, for a plunging liquid jet with the experimentally evaluated Q_{air} for a bubble cloud.

Acknowledgments

The authors wish to acknowledge the assistance of Mr. Hai Vu in developing the IVFM and the support of the Office of Naval Research under grant number N00014-94-1-1210, technical monitor Dr. Edwin Rood.

Nomenclature

d = upstream depth or model draft (m)
d_c = bubble cloud diameter (cm)
$\mathbf{F}$ = Froude number based on upstream conditions, $\mathbf{F} = U/\sqrt{gd}$
g = gravitational acceleration (m/s^2)
l = bubble chord length (mm)
Q = volume flow rate (m^3/s)
t = time (s)
U = upstream velocity (m/s)
V_{air} = total volume of air per unit streamwise distance (cm^3/cm)
x = streamwise coordinate (cm)
x^* = streamwise coordinate measured from impact line origin (cm)
y = cross stream coordinate (cm)
z = vertical coordinate (cm)
α = void fraction (percent)
ΔT = pulse width (s)
ϕ = dihedral angle (degrees)
θ = wedge half angle (degrees)

References

[1] Blanchard, D. C., and Woodcock, A. H., 1957, ‘‘Bubble Formation and Modification in the Sea and its Meteorological Significance,’’ Tellus, **9**, No. 2, pp. 145–158.
[2] Lamarre, E., and Melville, W. K., 1991, ‘‘Air Entrainment and Dissipation in Breaking Waves,’’ Nature (London), **351**, pp. 469–472.
[3] Lamarre, E., and Melville, W. K., 1994, ‘‘Void fraction measurements and sound-speed fields in bubble plumes generated by breaking waves,’’ J. Acoust. Soc. Am., **95**, No. 3, pp. 1317–1328.
[4] Lamarre, E., and Melville, W. K., 1992, ‘‘Instrumentation for the Measurement of Void-Fraction in Breaking Waves: Laboratory and Field Results,’’ IEEE J. Ocean Eng., **17**, No. 2, pp. 204–215.
[5] Cipriano, R. J., and Blanchard, D. C., 1981, ‘‘Bubble and Aerosol Spectra Produced by a Laboratory Breaking Wave,’’ J. Geophys. Res., **86**, pp. 8085–8092.
[6] Loewen, M. R., O’Dor, M. A., and Skafel, M. G., 1996, ‘‘Bubbles Entrained by Mechanically Breaking Waves,’’ J. Geophys. Res., **101**, pp. 20759–20769.
[7] Cartmill, J. W., and Su, M. Y., 1993, ‘‘Bubble size distribution under saltwater and freshwater breaking waves,’’ Dyn. Atmos. Oceans, **20**, pp. 25–31.
[8] Chanson, H., and Cummings, P. D., 1994, ‘‘Modeling Air Entrainment in Plunging Breakers,’’ Int. Symp.: Waves-Physical and Numerical Modeling, Vancouver, Canada, June.
[9] Biń, A. K., 1993, ‘‘Gas entrainment by plunging liquid jets,’’ Chem. Eng. Sci., **48**, No. 21, pp. 3585–3630.
[10] Chanson, H., and Cummings, P. D., 1994, ‘‘Effects of plunging breakers on the gas contents in the ocean,’’ Mar. Technol. Soc. J., **28**, No. 3, pp. 22–32.
[11] Waniewski, T. A., 1999, ‘‘Air Entrainment by Bow Waves,’’ Ph.D. thesis, Calif. Instit. of Tech.
[12] Chanson, H., 1988, ‘‘A study of air entrainment and aeration devices on a spillway model,’’ Ph.D. thesis, Univ. of Canterbury.
[13] Kytomaa, H. K., 1987, ‘‘Stability of the Structure in Multicomponent Flow,’’ Ph.D. thesis, Calif. Instit. of Tech., Pasadena, CA.
[14] Ishii, M., 1975, *Thermo-Fluid Dynamic Theory of Two-Phase Flow*, Eyrolles, Paris.
[15] Teyssedou, A., Tapucu, A., and Lortie, M., 1988, ‘‘Impedance probe to measure local void fraction profiles,’’ Rev. Sci. Instrum., **59**, No. 4, pp. 631–638.
[16] Prosperetti, A., and Oguz, H. N., 1993, ‘‘The impact of drops on liquid surfaces and the underwater noise of rain,’’ Annu. Rev. Fluid Mech., **25**, pp. 577–602.
[17] Chanson, H., 1995, ‘‘Air Bubble Entrainment in Free-Surface Turbulent Flows,’’ Tech. rept. CH46/95. Univ. of Queensland, June.
[18] Van de Sande, E., and Smith, J. M., 1976, ‘‘Jet break-up and air entrainment by low velocity turbulent water jets,’’ Chem. Eng. Sci., **31**, pp. 219–224.
[19] Carrica, P. M., Bonetto, F., Drew, D., and Lahey, Jr., R. T., 1998, ‘‘A Polydisperse Approach to the Two-Phase Flow Around a Ship,’’ Third Int. Conf. on Multiphase Flow, Lyon, France, June.